# Decoupling the roles of cell shape and mechanical stress in orienting and cueing epithelial mitosis

Alexander Nestor-Bergmann[1,2*§], Georgina A. Stooke-Vaughan[1*], Georgina K. Goddard[1*], Tobias Starborg[1], Oliver E. Jensen[2], Sarah Woolner[1§]

Affiliations:

1: Wellcome Trust Centre for Cell-Matrix Research, Division of Developmental Biology and Medicine, School of Medical Sciences, Faculty of Biology, Medicine & Health, Manchester Academic Health Science Centre, University of Manchester, Oxford Road, Manchester M13 9PT UK

2: School of Mathematics, University of Manchester, Manchester M13 9PL, UK

* These authors contributed equally to the work

§ Corresponding authors

## Abstract

Distinct mechanisms involving cell shape and mechanical force are known to influence the rate and orientation of division in cultured cells. However, uncoupling the impact of shape and force in tissues remains challenging. Combining stretching of *Xenopus laevis* tissue with a novel method of inferring relative mechanical stress, we find separate roles for cell shape in orientating division and mechanical stress in cueing division. We demonstrate that division orientation is best predicted by an axis of cell shape defined by the position of tricellular junctions, which aligns exactly with the principal axis of local cell stress rather than the tissue-level stress. The alignment of division to cell shape requires functional cadherin, but is not sensitive to relative cell stress magnitude. In contrast, cell proliferation rate is more directly regulated by mechanical stress, being correlated with relative isotropic stress, and can be decoupled from cell shape when myosin II is depleted.

## INTRODUCTION

Cell division orientation and timing must be carefully regulated in order to shape tissues and determine cell fate, preventing defective embryonic development and diseases such as cancer [1-3]. Recent work has shown that mechanical cues from the extracellular environment can influence cell division rate [4,5] and orientation [6-9]. What remains unclear is whether dividing cells are directly sensing mechanical forces or are responding to changes in cell shape induced by these forces. This distinction is crucial as the molecular mechanisms involved in either shape- or force-sensing could be very different [10,11].

Several mechanisms of division orientation control have been postulated in single cells, with evidence for both shape- and stress-sensing[7,12-14]. There is limited understanding of how these models could apply to tissues, where cells are linked together by adhesions and it is far more difficult to exclusively manipulate either cell shape or mechanical stress. Recent evidence for a shape-sensing mechanism was found in the *Drosophila* pupal notum. The spindle orientation protein, Mud (*Drosophila* orthologue of NuMA), localises at tricellular junctions, recruiting force generators to orient astral microtubules in rounding mitotic cells[15]. However, this mechanism has yet to be demonstrated in another system or related to mechanical stress. In contrast, recent work in a stretched monolayer of MDCK cells has indicated that division orientation may be mediated by a tension-sensing mechanism requiring E-cadherin, although an additional role for cell shape sensing could not be excluded[16]. Indeed, divisions in MDCK cells have also been found to align better with cell shape than a global stretch axis, though local cell stress was not known in this case [17].

Separating the roles of shape and stress in tissues will inevitably require an understanding of how force is distributed through heterogeneous cell layers. Experimental methods of assessing stress include laser ablation, atomic force microscopy and micro-aspiration [9,18-20]. Whilst informative, these techniques are invasive, perturbing the stress field through the measurement, and usually require constitutive modelling for the measurement to be interpreted [21,22]. However, mathematical modelling combined with high quality fluorescence imaging now provides the possibility of non-invasively inferring mechanical stress in tissues [23-28].

In this article, we apply a reproducible strain to embryonic *Xenopus laevis* tissue to investigate the roles of shape and stress in cell division in a multi-layered tissue. We particularly focus on mathematically characterising local (cell-level) and global (tissue-level) stress and the relation to cell shape and division. Our data suggest that mechanical stress is not directly sensed for orienting the mitotic spindle, acting only to deform cell shape, but is more actively read as a cue for mitosis.

## RESULTS

### Application of tensile force to a multi-layered embryonic tissue

To investigate the relationship between force, cell shape and cell division in a complex tissue, we developed a novel system to apply reproducible mechanical strain to a multi-layered embryonic tissue. Animal cap tissue was dissected from Stage 10 *Xenopus laevis* embryos and cultured on a fibronectin-coated elastomeric PDMS substrate (Figure 1A). A uniaxial stretch was applied to the PDMS substrate using an automated stretch device (Figure 1A), and imaged using standard microscopy. The three-dimensional structure of the stretched tissue (assessed using 3View EM) could be seen to comprise of approximately three cell layers (Figure 1B), as would be expected in a stage 10 *Xenopus laevis* embryo [29,30], therefore maintaining the multi-layered tissue structure present *in vivo.*

### Stretching elongates cell shape and reorients divisions.

A 35% stretch of the PDMS substrate led to a 19.67 ± 1.91% (95% confidence interval) elongation of apical cells in the animal cap along the stretch axis (measured change in length of 1-dimensional lines drawn on opposite sides of the animal cap; displacement field shown in Figure 1C). The difference in elongation between substrate and apical cells is presumably a result of the mechanical stress being dissipated through multiple cell layers. The qualitative change in cell shape was not as substantial as was previously observed in stretched monolayers[17] (Figure 1D).

We mathematically characterised shape using two parameters: orientation of the principal axis of cell shape relative to the stretch axis (0º), $\theta_A$, and cell circularity, $C_A$ (derived in Section 1 of the Supplementary Document). $C_A$ describes the degree of elongation of a cell (ranging from 0 being a straight line to 1 being a perfect circle) and $\theta_A$ indicates the principal direction in which this occurs. Stretching orients the majority of cells with the direction of stretch (Figure 1E) and causes a highly reproducible elongation of cell shape (Figure 1F). However, when the substrate was held fixed following stretch, cell elongation reduced over time and returned close to the unstretched shape profile after 90 minutes (95% confidence intervals of stretched animal caps at t = 90 minutes overlap with unstretched caps; Figure 1F). Therefore, cells in this tissue adapt to the elongation caused by stretching and do not behave like a purely elastic material.

In unstretched tissue, division orientation, $\theta_D$, was not significantly different from a uniform distribution ($p = 0.36$, Kolmogorov-Smirnov test; Figure 1G). In contrast, divisions in the stretched tissue were significantly oriented along the axis of stretch, ($p < 1.43\times10^{-9}$, Kolmogorov-Smirnov test; Figure 1G), with 52% of divisions oriented within 30º of the stretch axis (compared to 36% in unstretched).

**Shape-based models of division differ significantly depending on the cellular characteristics used to define shape**

A shape-based 'long axis' division rule may explain why stretching reorients divisions. However, the precise molecular mechanism behind shape-based models remains unclear and may vary across cell type and tissue context [7,9,13]. Past models have used different characteristics to determine the shape of a cell, usually selecting one of the following: cell area, cell perimeter and tricellular junction location. Though often used interchangeably, these shape characteristics model different biological functions. We investigated their differences and determined if one characteristic predicts division orientation better than the others.

We modelled cell shape by area, perimeter and tricellular junctions to derive three respective measures of cell shape orientation, $\theta_A$, $\theta_P$, and $\theta_J$, and circularity, $C_A$, $C_P$, and $C_J$ (Supplementary Document Section 1). Cells tend to have $C_P > C_A > C_J$ i.e. shape generally appears less anisotropic using the perimeter-based measure. $C_A$ and $C_P$ (and correspondingly $\theta_A$ and $\theta_P$) are reasonably well correlated, while $C_J$ (and $\theta_J$) tends to coincide less well with the others (Figure 2A&B). Thus a cell that appears round by area and perimeter can have clear elongation as measured by tricellular junctions. This is intuitive for rounding mitotic cells, where tricellular junctions can be distributed non-uniformly around the circular periphery[15]. However, it is surprising that this can also be the case in cells with relatively straight edges (Figure 2A''). Notably, cells in the *Xenopus* animal cap do not undergo the dramatic mitotic cell rounding seen in some other systems[15] (Supplemental Figure 1A&B).

**Tricellular junction placement is a better predictor of division orientation than cell area or perimeter.**

Given that $\theta_A$, $\theta_P$, and $\theta_J$ are often highly correlated, division orientation is generally well predicted by all three. We therefore focused on cases in which the orientations of shape differed by at least 15°. In a pooled sample of 600 cells from stretched and unstretched tissue, Only 7 cells were found to have $|\theta_A - \theta_P| \geq 15°$. 58 satisfied $|\theta_A - \theta_J| \geq 15°$ and 60 satisfied $|\theta_P - \theta_J| \geq 15°$. In both cases, $\theta_J$ was a significantly better predictor of division angle than random ($p < 0.0162$ when $|\theta_A - \theta_J| \geq 15°$; $p < 0.0042$ when $|\theta_P - \theta_J| \geq 15°$; Mann-Whitney U test), but $\theta_A$ and $\theta_P$ were not (Figure 2C&D). Furthermore, $C_A$, $C_P$, and $C_J$ were all significantly higher in these subpopulations (Supplemental Figure 1C&D; 95% confidence intervals do not overlap), indicating that these cells are rounder, yet can still effectively orient their spindle in-line with their tricellular junctions. This result is strengthened considering that tricellular junctions provide fewer data points than area or perimeter, thus junctional data may more susceptible to geometric error than area and perimeter.

In unstretched tissue, cells which we classed as "rounded" ($C_A > 0.65$; Figure 2E) showed no significant correlation between $\theta_A$ and $\theta_D$ or $\theta_P$ and $\theta_D$, as could be expected from previous work[7]. However, $\theta_J$ was significantly aligned with division angle in these round cells, when

compared to random (p = 0.025, Mann-Whitney U test) (Figure 2F&G). This degree of sensitivity is striking and further demonstrates that tricellular junction-sensing could function effectively in round cells, which may have previously been thought to divide at random.

**Local cell shape aligns with local stress and predicts division orientation better than global stretch and stress**

Contrary to observations in monolayers[16], we found that cells in stretched tissue divide according to cell shape both when $\theta_J$ is oriented with (Figure 3A) and against (Figure 3B&C) the direction of stretch. These data indicate that global stretch direction is a poor predictor of division angle when compared to cell shape. However, little is known about the local stress distribution around cells subjected to a stretch, which may not coincide with global stress in such a geometrically heterogeneous material.

We extended a popular vertex-based model to mathematically characterise cell stress [24-26,28]. Predicted orientations of forces from the model have been found to be in accordance with laser ablation experiments [31,32], indicating that the model can provide a physically relevant description of cellular stresses. Our methodology allows relative cell stress to be inferred solely from the positions of cell vertices, without invasively altering the mechanical environment (Supplementary Document, Section 2). The model predicts that the orientation of cell shape based on tricellular junctions, $\theta_J$, aligns exactly with the principal axis of local stress[28] (Figure 3D). We demonstrated this computationally in stretched tissue by simulating a uniaxial stretch (Figure 3E-F). Following stretch, we see that local cell stress remains aligned with $\theta_J$, rather than the global stress along the x-axis. Much previous work assumes that the local axis of stress coincides with the global stress. Significantly, the model predicts that a stress-sensing mechanism would align divisions in the same direction as a shape-based mechanism (as in Figure 3B).

**The magnitude of cell stress does not correlate with the alignment of division angle and tricellular junction positioning**

If a stress-sensing mechanism were contributing to orienting division, we hypothesised that cells under higher net tension or compression might orient division more accurately with the principal axis of stress ($\theta_J$). We infer relative tension/compression using the isotropic component of stress, effective pressure ($P^{\text{eff}}$) [28]:

$$P^{\text{eff}} = \frac{\widetilde{A}}{\widetilde{A}_0} - 1 + \frac{\Gamma \widetilde{L}^2}{2\widetilde{A}} + \frac{\Lambda \widetilde{L}\sqrt{\widetilde{A}_0}}{4\widetilde{A}}$$

where $\widetilde{A}$ is cell area, $\widetilde{L}$ is perimeter, $\widetilde{A}_0$ is the preferred area and $(\Lambda, \Gamma)$ are model parameters, defined in Section 2 of the Supplementary Document and inferred from data [28]. Cells under net tension have $P^{\text{eff}} > 0$, whereas $P^{\text{eff}} < 0$ indicates net compression. We provide a novel method for estimating $\widetilde{A}_0$ in Section 3 of the Supplementary Document. A representative

segmentation, showing cells predicted to be under net tension and compression, from an unstretched experiment is given in Figure 3G. Interestingly, we found no correlation between the value of $P^{\mathrm{eff}}$ (relative isotropic stress) and the alignment of division orientation to $\theta_J$ ($|\theta_D - \theta_J|$) (Supplemental Figure 2A). Accordingly, we found that knockdown of the tension sensor, vinculin, in stretched tissue does not affect division orientation relative to $\theta_J$ (Supplemental Figure 2C).

The mechanical state of a cell may also be characterised by shear stress, ξ (defined as the eigenvalue of the deviatoric component of the stress tensor, see Section 2 of the Supplementary Document). Larger values of |ξ| indicate increased cellular shear stress. Again, we found no correlation between ξ and the alignment of division to $\theta_J$ (Supplemental Figure 2B).

Despite the lack of correlation with stress magnitude, cell shape anisotropy, measured by $C_J$, correlates significantly with $|\theta_D - \theta_J|$ ($p < 3.04\times10^{-10}$, Spearman rank correlation coefficient; Figure 3H), with elongated cells having $\theta_D$ aligned with $\theta_J$ significantly better than round cells ($p < 1.64 \times 10^{-8}$; Figure 3I).

**Cadherin is required for positioning the mitotic spindle relative to cell shape**

Immunofluorescence staining of β-catenin confirmed that adherens junctions were distributed along the apical cell cortex, but particularly concentrated at the meeting points of three or more cells (Supplemental Figure 3A). To test a functional requirement for adherens junctions in orienting the spindle, we focused on maternal C-cadherin (cadherin 3), which is expressed at the highest level in Stage 10-11 *Xenopus* embryos [33,34]. We used two constructs to manipulate C-cadherin in the tissue: C-cadherin FL -6xmyc (CdhFL: Full length C-cadherin with 6xmyc tags at the intracellular c-terminus) and C-cadherin ΔC -6xmyc (CdhΔC: C-cadherin with extracellular and transmembrane domains, but lacking the cytosolic domain) (Figure 4A)[35]. CdhFL- and CdhΔC-injected embryos developed normally up to Stage 10/11 (Figure 4B), but the majority of embryos failed to complete gastrulation[33] (and data not shown). We observed no change in the cumulative distribution of cell circularities in CdhFL- and CdhΔC-injected tissues compared to control tissue (Supplemental Figure 3B). We also saw no difference in the rate of cell divisions (data not shown).

CdhΔC-injected tissue was elongated by application of stretch (Figure 4C), but showed worse alignment of divisions to stretch direction compared to uninjected control and CdhFL-injected tissue (Figure 4D; Mann-Whitney U test $p < 0.0162$ for CdhΔC less than CdhFL). Moreover, unstretched CdhΔC-injected tissue showed a significant decrease in the alignment of division angle to $\theta_J$, when compared to uninjected controls (Figure 4E; $p < 0.016$ Kolmogorov-Smirnov test on distributions differing), though both were significantly different to random (control: $p < 3.6\times10^{-11}$; CdhΔC: $p < 4.3\times10^{-11}$; Kolmogorov Smirnov test). We overexpressed C-cadherin in

the cell cortex by injecting CdhFL, which led to an increased localisation of the adherens junction component, β-catenin, around the entire cell perimeter (Supplemental Figure 3A). Focussing on cells which satisfied $|\theta_P - \theta_J| \geq 15°$, we found the striking result that division orientation was now significantly well predicted by cell perimeter, but no longer by tricellular junctions (Figure 4F; $p < 0.0027$ for alignment $\theta_D$ to $\theta_P$, but not significant for $\theta_D$ to $\theta_J$; Mann-Whitney U test). Therefore, overexpression of CdhFL was sufficient to switch division orientation from alignment with tricellular junctions to alignment with the shape of the entire cortex.

**Cell division rate is temporarily increased following change in global stress**

Stretch elicited a reproducible and significant increase in cell division rate, with 6.47 ± 1.12 % of cells dividing per hour in the stretched tissue compared to 3.22 ± 0.55 % in unstretched tissue (Figure 5A, 95% confidence intervals do not overlap), as reported for cultured cells and monolayers [13,17,36]. We roughly classify two distinct periods of division after stretch; there is an initial period of high proliferation (8.1% cells undergoing division per hour; Figure 5B), which drops, after 40-60 minutes, to near-unstretched control levels (4.2% cells undergoing division per hour). Stretching increases apical tissue area by 6 ± 2.69% (95% confidence interval), and is predicted to increase global stress by increasing individual values of $P^{\mathrm{eff}}$. We sought to determine whether the increase in division rate is a response to these changes.

In both stretched and unstretched experiments, dividing cells had a larger area than the population, being about 22.7% and 25.7% larger on average respectively (Figure 5C). Similarly, the mean perimeter was significantly larger in the dividing cells by about 14.1% in unstretched and 13.8% in stretched (Figure 5D). However, there was no significant difference in the level of cell elongation in dividing cells (Supplemental Figure 2D). Crucially, we found that dividing cells were more likely to be under predicted net tension than compression (Figure 5E, more cells in red region). However, $P^{\mathrm{eff}}$ is correlated with cell area (though the two are not always equivalent), thus a further perturbation was required to separate their effects.

**Loss of myosin II reduces cell contractility**

We perturbed the mechanical properties of the tissue with targeted knockdown of non-muscle myosin II using a previously published morpholino[37]. As expected, myosin II knockdown disrupted cytokinesis, seen by the formation of 'butterfly' shaped nuclei, where daughter cells had not fully separated (Figure 6A&B). However, division rate and orientation could still be assessed using the same methods described for control tissue. Myosin II is known to generate contractility within a tissue[38-40]. Accordingly, we found evidence for reduced contractility in the myosin II MO tissue by observing that cells were much slower at adapting to stretch, remaining elongated for longer (compare Figure 6C to Figure 1F).

**Myosin II is required for mitotic entry in unstretched tissue**

Somewhat surprisingly, considering suggestions that myosin II may play a stress-sensing role in orienting the spindle[9], we found that alignment of division angle to stretch and $\theta_J$ was unaffected in myosin II knockdown experiments (Figure 6D&E). In contrast, proliferation rate was significantly affected, with divisions virtually ceasing in unstretched myosin II MO tissue. Strikingly, stretching the myosin II MO tissue increased the division rate to significantly higher levels (Figure 6F). Thus myosin II is required to cue cells into division in the unstretched tissue, but this can be partially overridden by applying an external loading. Unlike in control experiments, dividing cells in myosin II knockdown stretch experiments were not significantly larger than the population in area (Figure 6G) or perimeter (Figure 6H). This suggests that cell area has been uncoupled as a cue to divide in the myosin II knockdowns.

## DISCUSSION

Previous models of cell division have demonstrated that specific features of cell shape, such as the cell cortex or tricellular junctions, may be important in orienting the spindle [7,15,41,42]. We have presented a framework for characterising cell shape in terms of its area, perimeter or tricellular junctions (Supplementary Document). We find that the principal axis of shape defined by tricellular junctions is the best predictor of division angle and aligns exactly with the principal axis of local stress. However, division angle is not better predicted in cells with higher/lower relative isotropic or shear stress and is unaffected by knockdown of vinculin in stretched tissue. This finding shares similarities with observations in the *Drosophila* pupal notum, where tricellular junctions have been hypothesised to localise force generators [15]. Notably, however, *Xenopus* animal cap cells do not undergo the dramatic mitotic rounding exhibited by cells in the notum.

Cell-cell adhesion has been linked to spindle orientation in MDCK cells, where E-cadherin instructs LGN/NuMA assembly at cell-cell contacts to orient divisions [43]. E-cadherin polarises along a stretch axis, reorienting divisions along this axis rather than according to cell shape [16]. In accordance, we find division is less well predicted by shape in embryos injected with C-cadherin ΔC -6xmyc, lacking the cytosolic domain. Interestingly, over-expression of C-cadherin around the entire cell cortex leads to division being best predicted by a perimeter-based shape axis. As $\beta$-catenin is increased around the cell cortex, this may be due to recruitment of spindle orientation proteins, such as NuMA/LGN [43]. We, and others, find that cadherin is most highly localised at the meeting points between three or more cells in wild-type *Xenopus* epithelium [35]. We suggest that these “hotspots” of cadherin localisation recruit spindle orientation machinery such as LGN/NuMA, reminiscent of the Mud-dependent tricellular junction-sensing mechanism in the *Drosophila* pupal notum [15].

306 Stretching increases proliferation rate, which correlates with cell area, perimeter and effective
307 pressure. We see almost no proliferation in unstretched myosin II MO experiments, although,
308 rather strikingly, the division rate is significantly increased following stretch. Dividing myosin II
309 MO cells are not significantly larger in area or perimeter than the population as a whole,
310 indicating that cell area has been decoupled as a division cue. Considering the established
311 role of myosin II as a force generator [39,40,44], it is possible that the myosin II MO cells cannot
312 generate enough internal contractility in neighbouring cells to engage the mechanical cues
313 required for mitotic entry. Myosin II has also been shown to function in stress-sensing
314 pathways [45,46], which may explain why the proliferation rate in stretched myosin II MO cells
315 does not reach the levels of stretched controls. Contrary to findings in other systems [9], loss of
316 myosin II does not alter division orientation relative to cell shape.
317
318 In conclusion, we have combined whole-tissue stretching with a biomechanical model to
319 propose separate roles for cell shape and mechanical stress in orienting the spindle and
320 cueing mitosis (summarised in Figure 7). The mechanism involved in orienting the mitotic
321 spindle does not appear to sense relative cell stress directly. Instead, division is best
322 predicted by an axis of shape defined by tricellular junctions and is dependent on functional
323 cadherin. In contrast to this shape-based mechanism, we find that cells may directly sense
324 mechanical stress as a cue for mitotic entry, in a myosin II-dependent manner.
325

## 326 Materials and Methods

327

### 328 *Xenopus laevis* embryos and microinjection

329 *Xenopus laevis* embryos were obtained and injected as described previously[47]. RNA was
330 synthesised as described previously [48] and microinjected at the following needle
331 concentrations: 0.5 mg/ml GFP-α-tubulin; 0.1 mg/ml cherry-histone2B[49]; 0.125 mg/ml
332 cadherin 3a full length:6x myc-tag; 0.125 mg/ml cadherin 3a deleted cytosolic domain:6x myc-
333 tag[35]. Morpholinos prepared as 1mM stocks (diluted in water) were heated at 65°C for 5
334 minutes and microinjected at a needle concentration of 1mM and needle volume of 2.5nl into
335 all cells of four-cell stage embryos. The morpholinos used were MHC-B (Myosin Heavy
336 Chain-B, myosin II) MO (5'-CTTCCTGCCCTGGTCTCTGTGACAT-3'; [37]), Vinculin MO (5'-
337 TATGGAAGACCGGCATCTTGGCAAT-3'); [50]) and standard control MO (5'-
338 CCTCTTACCTCAGTTACAATTTATA-3'; Gene Tools LLC). All embryos were incubated at
339 16°C for approximately 20 hours prior to animal cap dissection.

340

### 341 Animal cap dissection and culture

342 Animal cap tissue was dissected from the embryo at stage 10 of development (early gastrula
343 stage) following a previously described protocol [51], and cultured in Danilchik's for Amy explant
344 culture media (DFA; 53mM $NaCl_2$, 5mM $Na_2CO_3$, 4.5mM Potassium gluconate, 32mM
345 Sodium gluconate, 1mM $CaCl_2$, 1mM $MgSO_4$) on a 20mm × 20mm elastomeric PDMS

346 (Sylgard 184, SLS) membrane made in a custom mold and coated with fibronectin (fibronectin
347 from bovine plasma, Sigma). Explants were held in place by a coverslip fragment. Each
348 membrane was then incubated at 18°C for at least 2 hours prior to imaging.
349
350 **Animal cap stretch manipulation and confocal imaging**
351 Each PDMS membrane was attached to a stretch apparatus (custom made by Deben UK
352 Limited) fixed securely to the stage of a Leica TCS SP5 AOBS upright confocal and a 0.5mm
353 (to remove sag on the membrane) or 8.6mm uniaxial stretch was applied for unstretched and
354 stretched samples respectively.
355
356 Images were collected on a Leica TCS SP5 AOBS upright confocal using a 20x/0.50 HCX
357 Apo U-V-I (W (Dipping Lens)) objective and 2x confocal zoom. The distance between optical
358 sections was maintained at 4.99μm and the time interval between each frame was 20
359 seconds, with each samples being imaged for up to 2.5 hours. Maximum intensity projections
360 of these 3D stacks are shown in the results.
361
362 **Image analysis**
363 Image analysis was performed using ImageJ [52]. Cell division orientation was quantified using
364 the straight-line tool to draw a line between the dividing nuclei of a cell in late anaphase (a
365 stage in mitosis where division orientation is set and the spindle undergoes no further rotation
366 [47,53]). Using the ROI manager the angle of division relative to stretch (horizontal axis) was
367 recorded along with the frame and location of the division. Single cell edges and junctions
368 were manually traced 40s before NEB using the freehand paintbrush tool. The whole
369 population of cells in the apical layer of the animal cap was manually traced, along with
370 peripheral junctions and cell centres, using the freehand paintbrush tool. Segmentation of the
371 cell boundaries was performed using in-house Python scripts implementing a watershed
372 algorithm. Geometric features of the cells, such as area and perimeter, were extracted and
373 analysed in Python. For further details on how cell shape was characterised using the
374 segmented images, please see the Supplementary Document.
375
376 **Data analysis**
377 The data analysis and plotting was carried out using in-house Python scripts. Statistical tests
378 were performed using the SciPy library [54]. Mann-Whitney U tests were used to assess if rose
379 histograms were distributed closer to zero. Kolmogorov-Smirnov tests were used to assess if
380 two distributions were significantly different. Otherwise, bootstrapping with 95% confidence
381 intervals, which allow the precision of the estimate to be seen[55], were used to assess
382 significance.
383
384 **Immunofluorescence**

Embryos were fixed at stage 12 following the protocol previously detailed by Jones et al., (2014)[56]. Embryos were incubated in primary and secondary antibodies in TBSN/BSA (Tris-buffered saline: 155mM NaCl, 10mM Tris-Cl [pH 7.4]; 0.1% Nonidet P-40; 10 mg/ml BSA) overnight at 4°C, with five 1 hour washes with TBSN/BSA following each incubation. Primary antibodies were: anti-β-catenin at 1:200 dilution, raised in rabbit (Abcam) and anti c-myc 9E10 at 1:1000 dilution, raised in mouse (Santa-cruz). Alexa Fluor secondary antibodies, anti-rabbit 488 and anti-mouse 568 (Invitrogen) were used at a dilution of 1:400. After staining, embryos were methanol dehydrated, then cleared and mounted in Murray's Clear (2:1, benzyl benzoate:benzyl alcohol; [57]).

Images were collected on a Leica TCS SP5 AOBS inverted confocal using a 63x HCX PL APO (Oil $\lambda$ BL) objective and 1024 x 1024 format. Single confocal slices are shown in the results.

**Implementation of the vertex-based model**

The numerical simulations of the vertex-based model were carried out using the same scripts outlined in section 3.8 of [28]. Model parameters used for all simulations were $(\Lambda, \Gamma) = (-0.259, 0.172)$, determined using a fitting procedure described in [28].

**Acknowledgements**

ANB was supported by a BBSRC studentship. SW, GSV and GG were supported by a Wellcome Trust/Royal Society Sir Henry Dale Fellowship to SW [098390/Z/12/Z] with additional funding from the Wellcome Trust ISSF [105610/Z/14/Z]. The Bioimaging Facility microscopes used in this study were purchased with grants from BBSRC, Wellcome and the University of Manchester Strategic Fund. Thanks to Peter March and Roger Meadows for their help with the microscopy and to Lance Davidson for sharing Cadherin constructs. Also, special thanks to Viki Allan, Tom Millard and Nancy Papalopulu for their critical reading of the manuscript.

## Bibliography

1. Quyn, A. J. *et al.* Spindle Orientation Bias in Gut Epithelial Stem Cell Compartments Is Lost in Precancerous Tissue. *Cell Stem Cell* **6,** 175–181 (2010).
2. Pease, J. C. & Tirnauer, J. S. Mitotic spindle misorientation in cancer – out of alignment and into the fire. *J Cell Sci* **124,** 1007–1016 (2011).
3. Mishra, P. & Chan, D. C. Mitochondrial dynamics and inheritance during cell division, development and disease. *Nature Reviews Molecular Cell Biology* **15,** 634–646 (2014).
4. Streichan, S. J., Hoerner, C. R., Schneidt, T., Holzer, D. & Hufnagel, L. Spatial constraints control cell proliferation in tissues. *PNAS* **111,** 5586–5591 (2014).
5. Benham-Pyle, B. W., Pruitt, B. L. & Nelson, W. J. Mechanical strain induces E-cadherin-dependent Yap1 and beta-catenin activation to drive cell cycle entry. *Science* **348,** 1024–1027 (2015).
6. Mao, Y. *et al.* Planar polarization of the atypical myosin Dachs orients cell divisions in

Drosophila. *Genes Dev.* **25,** 131–136 (2011).
7. Minc, N., Burgess, D. & Chang, F. Influence of cell geometry on division-plane positioning. *Cell* **144,** 414–426 (2011).
8. Legoff, L., Rouault, H. & Lecuit, T. A global pattern of mechanical stress polarizes cell divisions and cell shape in the growing Drosophila wing disc. *Development* **140,** 4051–4059 (2013).
9. Campinho, P. *et al.* Tension-oriented cell divisions limit anisotropic tissue tension in epithelial spreading during zebrafish epiboly. *Nature cell biology* **15,** 1405–1414 (2013).
10. Nestor-Bergmann, A., Goddard, G. & Woolner, S. Force and the spindle: Mechanical cues in mitotic spindle orientation. *Semin. Cell Dev. Biol.* **34,** 133–139 (2014).
11. Luo, T., Mohan, K., Iglesias, P. A. & Robinson, D. N. Molecular mechanisms of cellular mechanosensing. *Nature Materials* **12,** 1063–1070 (2013).
12. Minc, N. & Piel, M. Predicting division plane position and orientation. *Trends in Cell Biology* **22,** 193–200 (2012).
13. Fink, J. *et al.* External Forces Control Mitotic Spindle Positioning. *Nature cell biology* **13,** 771–778 (2011).
14. Théry, M., Pépin, A., Dressaire, E., Chen, Y. & Bornens, M. Cell distribution of stress fibres in response to the geometry of the adhesive environment. *Cell Motility and the Cytoskeleton* **63,** 341–355 (2006).
15. Bosveld, F. *et al.* Epithelial tricellular junctions act as interphase cell shape sensors to orient mitosis. *Nature* **530,** 495–+ (2016).
16. Hart, K. C. *et al.* E-cadherin and LGN align epithelial cell divisions with tissue tension independently of cell shape. *Proc. Natl. Acad. Sci. U.S.A.* **114,** E5845–E5853 (2017).
17. Wyatt, T. P. J. *et al.* Emergence of homeostatic epithelial packing and stress dissipation through divisions oriented along the long cell axis. *PNAS* **112,** 5726–5731 (2015).
18. Hutson, M. S. *et al.* Forces for morphogenesis investigated with laser microsurgery and quantitative modeling. *Science* **300,** 145–149 (2003).
19. Hoh, J. H. & Schoenenberger, C. A. Surface morphology and mechanical properties of MDCK monolayers by atomic force microscopy. *J Cell Sci* **107 ( Pt 5),** 1105–1114 (1994).
20. Davidson, L., Dassow, von, M. & Zhou, J. Multi-scale mechanics from molecules to morphogenesis. *Int. J. Biochem. Cell Biol.* **41,** 2147–2162 (2009).
21. Stooke-Vaughan, G. A., Davidson, L. A. & Woolner, S. Xenopus as a model for studies in mechanical stress and cell division. *Genesis* **55,** e23004 (2017).
22. Sugimura, K., Lenne, P.-F. & Graner, F. Measuring forces and stresses in situ in living tissues. *Development* **143,** 186–196 (2016).
23. Xu, G.-K., Liu, Y. & Li, B. How do changes at the cell level affect the mechanical properties of epithelial monolayers? *Soft Matter* **11,** 8782–8788 (2015).
24. Brodland, G. W. *et al.* CellFIT: A Cellular Force-Inference Toolkit Using Curvilinear Cell Boundaries. *PLoS ONE* **9,** e99116 (2014).
25. Ishihara, S. & Sugimura, K. Bayesian inference of force dynamics during morphogenesis. *J. Theoret. Biol.* **313,** 201–211 (2012).
26. Chiou, K. K., Hufnagel, L. & Shraiman, B. I. Mechanical stress inference for two dimensional cell arrays. *PLoS Comput. Biol.* **8,** e1002512 (2012).
27. Feroze, R., Shawky, J. H., Dassow, von, M. & Davidson, L. A. Mechanics of blastopore closure during amphibian gastrulation. *Dev. Biol.* **398,** 57–67 (2015).
28. Nestor-Bergmann, A., Goddard, G., Woolner, S. & Jensen, O. Relating cell shape and mechanical stress in a spatially disordered epithelium using a vertex-based model. *Math. Med. Biol.* (2017). doi:10.1093/imammb/dqx008
29. Keller, R. E. & Schoenwolf, G. C. An SEM study of cellular morphology, contact, and arrangement, as related to gastrulation inXenopus laevis. *Development Genes and Evolution* (1977).
30. Keller, R. E. The cellular basis of epiboly: an SEM study of deep-cell rearrangement during gastrulation in Xenopus laevis. *J Embryol Exp Morphol* **60,** 201–234 (1980).
31. Farhadifar, R., Röper, J. C., Aigouy, B., Eaton, S. & Jülicher, F. The influence of cell mechanics, cell-cell interactions, and proliferation on epithelial packing. *Current Biology* **17,** 2095–2104 (2007).
32. Landsberg, K. P. *et al.* Increased Cell Bond Tension Governs Cell Sorting at the

Drosophila Anteroposterior Compartment Boundary. *Current Biology* **19,** 1950–1955 (2009).

33. Lee, C. H. & Gumbiner, B. M. Disruption of Gastrulation Movements in Xenopus by a Dominant-Negative Mutant for C-Cadherin. *Dev. Biol.* **171,** 363–373 (1995).
34. Heasman, J. *et al.* A Functional Test for Maternally Inherited Cadherin in Xenopus Shows Its Importance in Cell-Adhesion at the Blastula Stage. *Development* **120,** 49–57 (1994).
35. Kurth, T. *et al.* Immunocytochemical studies of the interactions of cadherins and catenins in the early Xenopus embryo. *Dev. Dyn.* **215,** 155–169 (1999).
36. Streichan, S. J., Hoerner, C. R., Schneidt, T., Holzer, D. & Hufnagel, L. Spatial constraints control cell proliferation in tissues. *PNAS* **111,** 5586–5591 (2014).
37. Skoglund, P., Rolo, A., Chen, X., Gumbiner, B. M. & Keller, R. Convergence and extension at gastrulation require a myosin IIB-dependent cortical actin network. *Development* **135,** 2435–2444 (2008).
38. Effler, J. C. *et al.* Mitosis-Specific Mechanosensing and Contractile-Protein Redistribution Control Cell Shape. *Current Biology* **16,** 1962–1967 (2006).
39. Clark, A. G., Wartlick, O., Salbreux, G. & Paluch, E. K. Stresses at the Cell Surface during Animal Cell Morphogenesis. *Current Biology* **24,** R484–R494 (2014).
40. Gutzman, J. H., Sahu, S. U. & Kwas, C. Non-muscle myosin IIA and IIB differentially regulate cell shape changes during zebrafish brain morphogenesis. *Dev. Biol.* **397,** 103–115 (2015).
41. Luxenburg, C., Pasolli, H. A., Williams, S. E. & Fuchs, E. Developmental roles for Srf, cortical cytoskeleton and cell shape in epidermal spindle orientation. *Nature cell biology* **13,** 203–U51 (2011).
42. Hertwig, O. Ueber den Werth der ersten Furchungszellen für die Organbildung des Embryo Experimentelle Studien am Frosch-und Tritonei. *Archiv f. mikrosk. Anat.* **42,** 662–807 (1893).
43. Gloerich, M., Bianchini, J. M., Siemers, K. A., Cohen, D. J. & Nelson, W. J. Cell division orientation is coupled to cell-cell adhesion by the E-cadherin/LGN complex. *Nat Commun* **8,** (2017).
44. Vicente-Manzanares, M., Ma, X., Adelstein, R. S. & Horwitz, A. R. Non-muscle myosin II takes centre stage in cell adhesion and migration. *Nature Reviews Molecular Cell Biology* **10,** 778–790 (2009).
45. Hirata, H. *et al.* Actomyosin bundles serve as a tension sensor and a platform for ERK activation. *EMBO Rep.* **16,** 250–257 (2015).
46. Priya, R. *et al.* Feedback regulation through myosin II confers robustness on RhoA signalling at E-cadherin junctions. *Nature cell biology* **17,** 1282–1293 (2015).
47. Woolner, S. & Papalopulu, N. Spindle Position in Symmetric Cell Divisions during Epiboly Is Controlled by Opposing and Dynamic Apicobasal Forces. *Developmental cell* **22,** 775–787 (2012).
48. Sokac, A. M., Co, C., Taunton, J. & Bement, W. Cdc42-dependent actin polymerization during compensatory endocytosis in Xenopus eggs. *Nature cell biology* **5,** 727–732 (2003).
49. Kanda, T., Sullivan, K. F. & Wahl, G. M. Histone-GFP fusion protein enables sensitive analysis of chromosome dynamics in living mammalian cells. *Current Biology* **8,** 377–385 (1998).
50. Petridou, N. I., Stylianou, P. & Skourides, P. A. A dominant-negative provides new insights into FAK regulation and function in early embryonic morphogenesis. *Development* **140,** 4266–4276 (2013).
51. Joshi, S. D. & Davidson, L. A. Live-cell imaging and quantitative analysis of embryonic epithelial cells in Xenopus laevis. *J Vis Exp* (2010). doi:10.3791/1949
52. Schneider, C. A., Rasband, W. S. & Eliceiri, K. W. NIH Image to ImageJ: 25 years of image analysis. *Nat. Methods* **9,** 671–675 (2012).
53. Woolner, S., O'Brien, L. L., Wiese, C. & Bement, W. M. Myosin-10 and actin filaments are essential for mitotic spindle function. *J Cell Biol* **182,** 77–88 (2008).
54. Jones, E. & Oliphant E, P. SciPy: Open Source Scientific Tools for Python. (2001). Available at: http://www.scipy.org/. (Accessed: 8 June 2017)
55. Nakagawa, S. & Cuthill, I. C. Effect size, confidence interval and statistical significance: a practical guide for biologists. *Biol Rev Camb Philos Soc* **82,** 591–605 (2007).

550 56. Jones, L. A. *et al.* Dynein light intermediate chains maintain spindle bipolarity by
551 functioning in centriole cohesion. *J. Cell Biol.* **207,** 499–516 (2014).
552 57. Klymkowsky, M. W. & Hanken, J. Whole-Mount Staining of Xenopus and Other
553 Vertebrates. *Methods in Cell Biology* **36,** 419–& (1991).
554

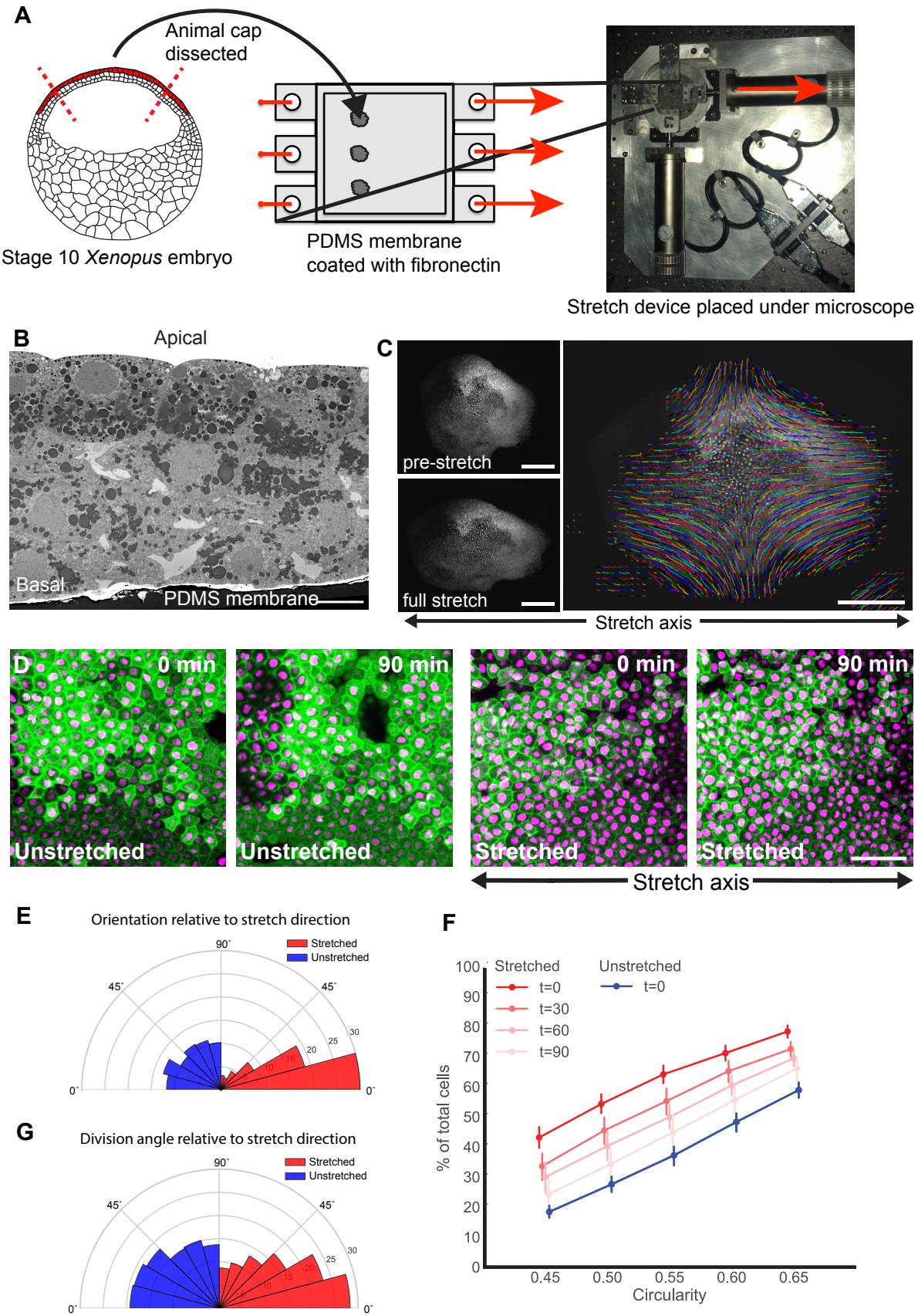


**Figure 1: Application of tensile force to a multi-layered tissue**. **A.** Animal cap tissue was dissected from Stage 10 Xenopus laevis embryos and adhered to fibronectin-coated PDMS membranes and a 35% uniaxial stretch of the membrane was applied. **B**. The animal cap tissue is 2-3 cells thick; cell shape and divsions were assessed in the apical cell layer. **C**. Displacement of nuclei was tracked in a stretched animal cap. **D**. Confocal images of the apical cells in unstretched and stretched animal caps (green: GFP-alpha-tubulin; magenta: cherry-histone2B), taken 0 and 90 minutes after stretch. **E**. Rose plot showing orientation of cell shape relative to direction of stretch in unstretched (blue) and stretched (red; measured immediately following stretch) experiments. **F**. Cumulative plots of cell circularity in unstretched (blue) and stretched (red; at 0, 30, 60 and 90 mins after stretch) animal caps (0=straight line; 1=circle). 100% of cells have circularity ≤ 1. Markers slightly off-set for clarity. **G.** Rose plot of division angle relative to direction of stretch for unstretched (red) and stretched (blue) experiments. Kolmogorov-Smirnov test indicates that the unstretched distribution is not significantly different from a uniform distribution, n = 343 divisions, 15 animal caps; Kolmogorov-Smirnov test indicates that stretched distribution is significantly different from uniform, $p < 1.4\times10^{-9}$, n = 552 divisions, 17 animal caps. Scale bar: 10μm in **B**, 500μm in **C**, 50μm in **D**.

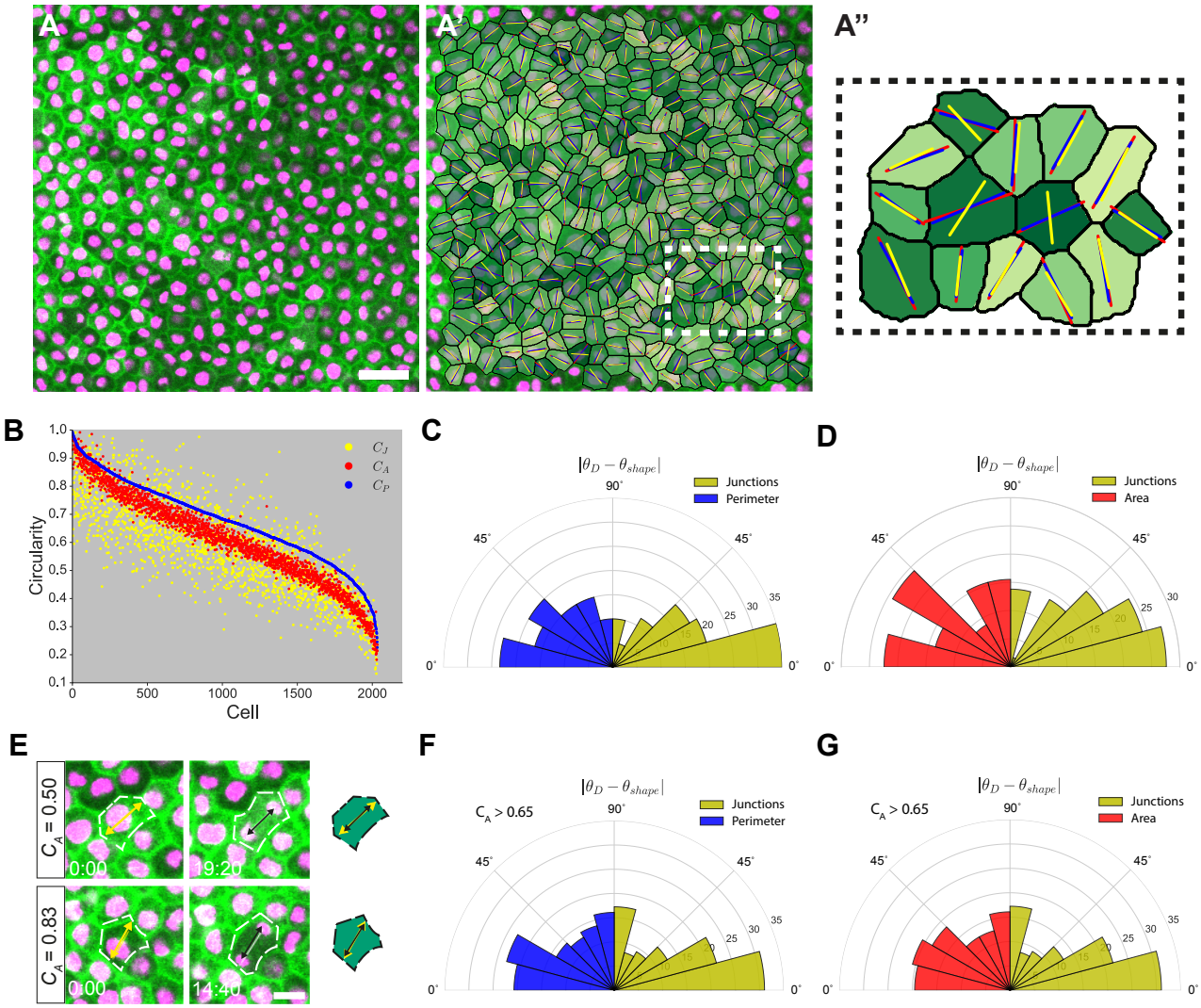


**Figure 2: Cell division orientation is best predicted by an axis of shape defined by tricellular junctions. A.** Representative image of control cells from an unstretched experiment. Scale bar: 20μm **A'.** Overlay of segmentation of cells given in **A**, with the principal axis of shape characterised by area, perimeter and junctions drawn in red, blue and yellow respectively. **A''.** Enlargement of segmented cells from white box drawn in **A'**. **B.** Circularities of 2035 cells from unstretched experiments, with shape characterised by area, perimeter and junctions plotted in red, blue and yellow respectively. Cells have been ordered in descending order of perimeter-based circularity ($C_P$), with the corresponding values of $C_A$ and $C_J$ plotted alongside. **C**. Rose plot of difference between division angle, $\theta_D$, and orientation of shape based on perimeter (blue; $\theta_{shape} = \theta_P$) and junctions (yellow; $\theta_{shape} = \theta_J$), for cells which satisfy $|\theta_P - \theta_J| \geq 15°$. **D.** Rose plot of difference between division angle, $\theta_D$, and orientation of shape based on area (red; $\theta_{shape} = \theta_A$) and junctions (yellow; $\theta_{shape} = \theta_J$), for cells which satisfy $|\theta_A - \theta_J| \geq 15°$. **E.** Examples of round (top) and elongated (bottom) cells where division angle (black arrows) is well predicted by the principal axis of shape defined by area (yellow arrows). **F.** Rose plot of difference between division angle, $\theta_D$, and orientation of shape based on perimeter (blue; $\theta_{shape} = \theta_P$) and junctions (yellow; $\theta_{shape} = \theta_J$), for round cells which satisfy $C_A > 0.65$. **G.** Rose plot of difference between division angle, $\theta_D$, and orientation of shape based on area (red; $\theta_{shape} = \theta_A$) and junctions (yellow; $\theta_{shape} = \theta_J$), for round cells which satisfy $C_A > 0.65$.

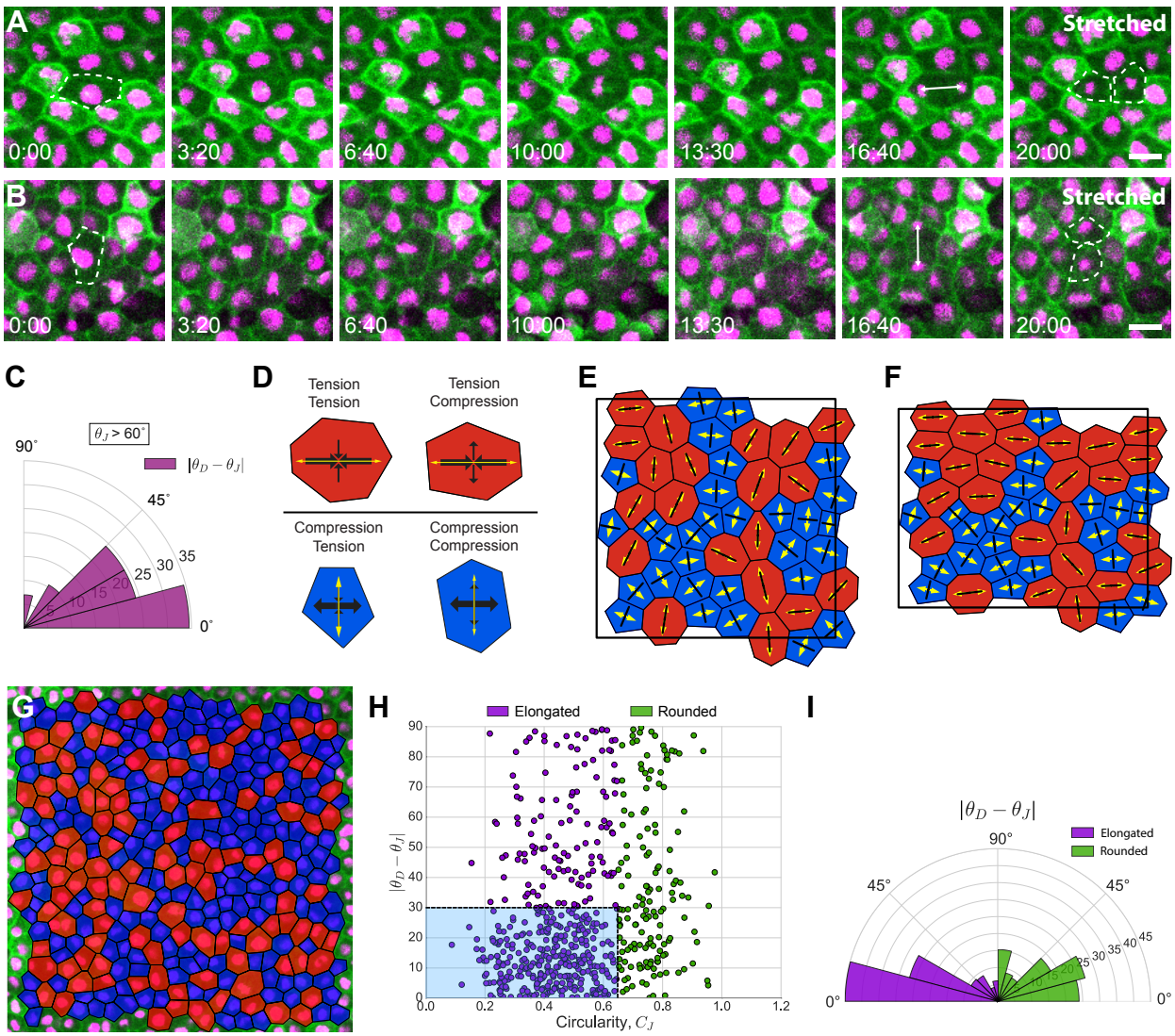


**Figure 3: Local stress aligns with shape. Division orientation is better predicted by shape in elongated cells, rather than those with higher relative isotropic or shear stress. A.** Images taken from a confocal timelapse movie of a division in a cell in stretched tissue whose interphase shape (dashed line, 0:00) is oriented with the stretch (horizontal) axis. Cell division aligns with both cell shape and stretch axis. **B.** Timelapse images of an unusual cell in a stretched tissue, whose interphase shape (dashed line, 0:00) is oriented against the stretch axis. Cell division aligns with cell shape but against the stretch axis. **C.** Rose plot of difference between division angle, $\theta_D$, and orientation of shape based on junctions, $\theta_J$, for cells from stretched experiments, where $\theta_J$ was at least $60^\circ$ divergent to the direction of stretch. 29 cells satisfied this condition. Kolmogorov-Smirnov test found a significant difference from a uniform distribution (p=0.022). **D.** Representative cells showing classification of cell stress configurations. Red (blue) cells are under net tension (compression), where $P^{\text{eff}}$ is positive (negative). Larger (smaller) black arrows indicate the orientation of the principal (secondary) axis of stress, with inward- (outward)-pointing arrows indicating the tension (compression) generated by the cell. Yellow arrows indicate the principal axis of shape defined by cell junctions, which aligns exactly with a principal axis of stress. **E.** 50 simulated cells randomly generated in a periodic box, relaxed to equilibrium with parameters $(\Lambda,\Gamma)$ = (-0.259, 0.172), under conditions of zero global stress (Nestor-Bergmann et al., 2017). Red (blue) cells are under net tension (compression). Principal axis of stress (shape) indicated in black (yellow). **F.** Cells from **E** following a 13% area-preserving uniaxial stretch along the x-axis. **G.** Example segmented cells from an unstretched experiment. Cells in red (blue) are predicted to be under net tension (compression). **H.** Cell circularity defined by junctions, $C_J$, vs $|\theta_D - \theta_J|$. Spearman rank correlation coefficient found a significant correlation ($p < 3.04 \times 10^{-10}$). Elongated cells ($C_J \leq 0.65$) cluster in blue box, whereas rounded cells ($C_J > 0.65$) have a more uniform distribution. **I.** Rose plot of difference between division angle, $\theta_D$, and orientation of shape based on junctions, $\theta_J$ for round ($C_J > 0.65$; right) and elongated ($C_J \leq 0.65$; left) cells shown in **H**. Mann-Whitney U test indicated that elongated cells have $\theta_J$ aligned significantly more with $\theta_D$ than rounded cells ($p < 1.64 \times 10^{-8}$). Scale bar in **A&B:** 20μm. All rose plots show percentage of cells.

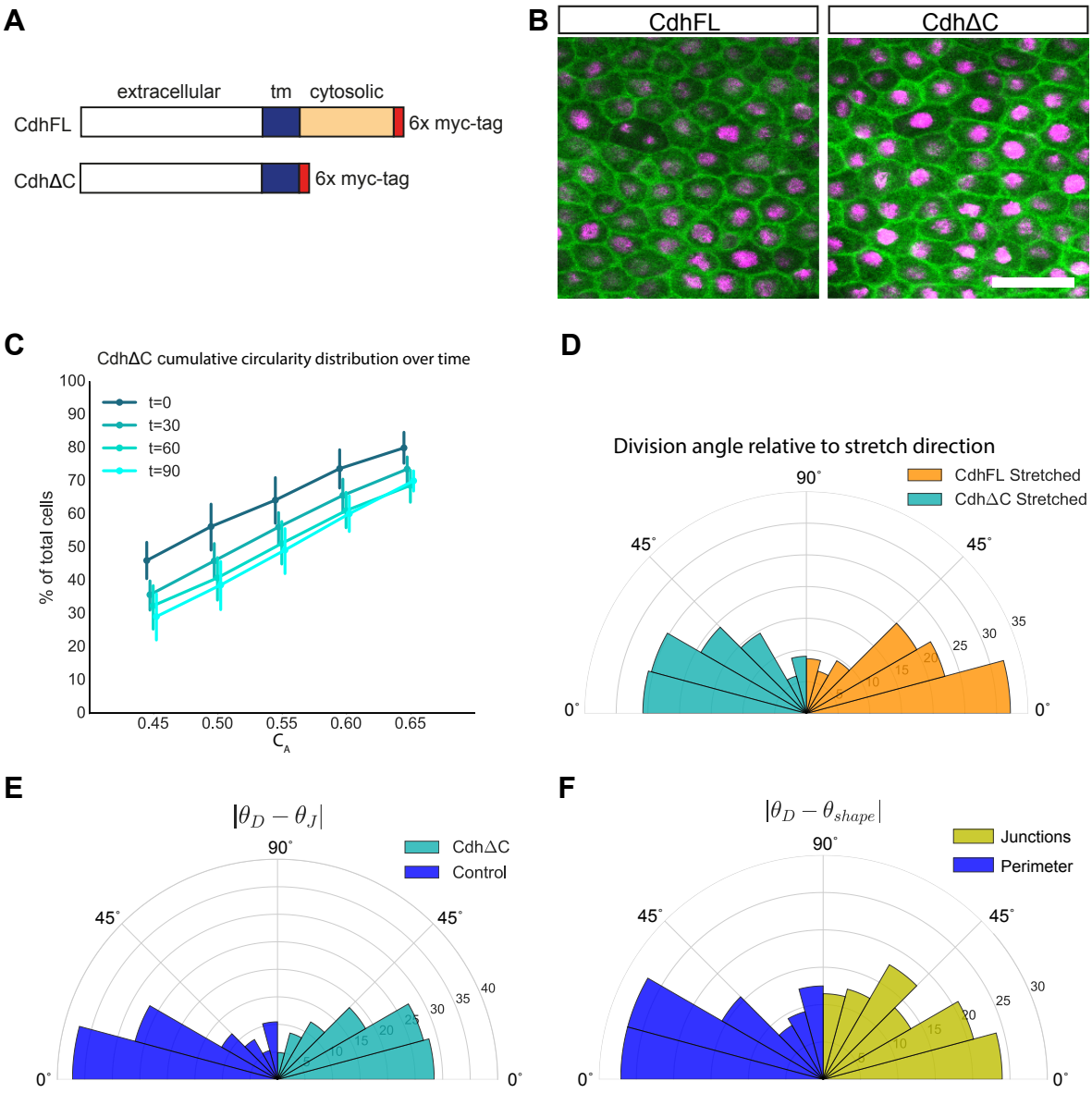


**Figure 4: C-Cadherin is involved in orienting the mitotic spindle according to cell shape. A.** Schematic of Cadherin contructs CdhFL and CdhΔC **B.** Images taken from a confocal timelapse movie of CdhFL- (left) and CdhΔC- (right) injected stretched animal cap explants. Scale bar 50μm. **C.** Cumulative plots of cell circularity defined by area, $C_A$, in CdhΔC-injected stretched animal caps at 0, 30, 60 and 90 mins after stretch (stretch applied just before 0 min). 100% of cells have $C_A < 1$. **D.** Rose plot of division angles, $\theta_D$, relative to direction of stretch for cells from stretched CdhΔC-injected (411 cells; cyan) and stretched CdhFL-injected experiments (552 cells; orange). CdhFL-injected cells align significantly better with direction of stretch ($p < 0.0162$, Mann-Whitney U test). **E.** Rose plot of difference between division angle, $\theta_D$, and orientation of shape based on junctions, $\theta_J$, for cells from CdhΔC-injected experiments (390 cells; cyan) and control experiments (239 cells; blue). Distributions are significantly different ($p < 0.016$ Kolmogorov-Smirnov test). **F.** Rose plot of difference between division angle, $\theta_D$, and orientation of shape based on perimeter, $\theta_P$, (blue) and junctions, $\theta_J$, (yellow) for 96 cells from CdhFL-injected experiments which satisfied $|\theta_P - \theta_J| \geq 15°$. $\theta_D$ aligns significantly better to $\theta_P$ than a random distribution ($p < 0.004$; Kolmogorov-Smirnov test), but not to $\theta_J$. Rose plots show percentage of cells.

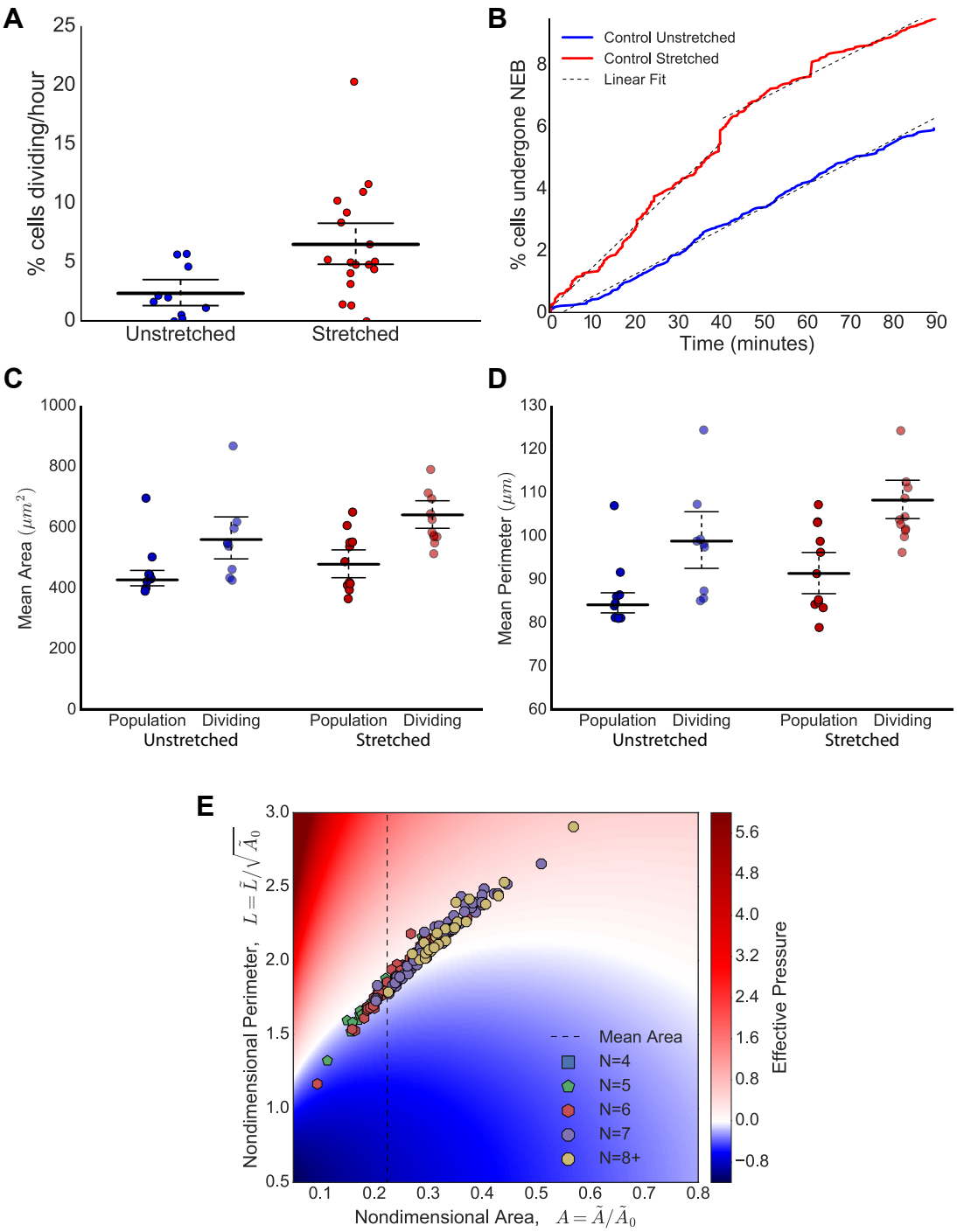


**Figure 5: Stretching increases division rate. Dividing cells have large area, perimeter and relative effective pressure. A.** Division rate (percentage of cells entering mitosis per hour) increases in stretched tissue compared to unstretched. 95% confidence intervals do not overlap, indicating significant difference. Each point represents the mean division rate from an animal cap. **B.** Percentage of cells that have undergone nuclear envelope breakdown (NEB) with respect to time in control stretched (red) and unstretched (blue) experiments from **A**. Dashed lines indicate linear lines of best fit; control unstretched experiments have gradient 4.2% cells undergoing division per hour. Stretched experiments have initial gradient 8.1% and then 4.35% cells undergoing division per hour. **C.** Comparison of mean area of population of all cells vs dividing cells from unstretched and stretched control experiments. Error bars represent mean and 95% confidence intervals, which do not overlap between the population and dividing cells, indicating a significant difference. **D.** Comparison of mean perimeter of population of all cells vs dividing cells from unstretched and stretched control experiments. Error bars represent mean and 95% confidence intervals, which do not overlap between the population and dividing cells, indicating a significant difference. **E.** Heat map showing predicted relative isotropic stress (effective pressure, $P^{\text{eff}}$) of dividing cells from control unstretched experiments. Areas and perimeters have been nondimensionalised using the preferred areas, $\tilde{A}_0$, fitted to each experiment in Supplemental Figure 4C. Polygonal class (number of neighbours) indicated by marker colour and style, with (4,5,6,7,8+) sided cells given in (blue, green, red, purple, yellow). Dashed vertical line represents mean area of all cells. Cells lying in red (blue) regions are under predicted net tension (compression).

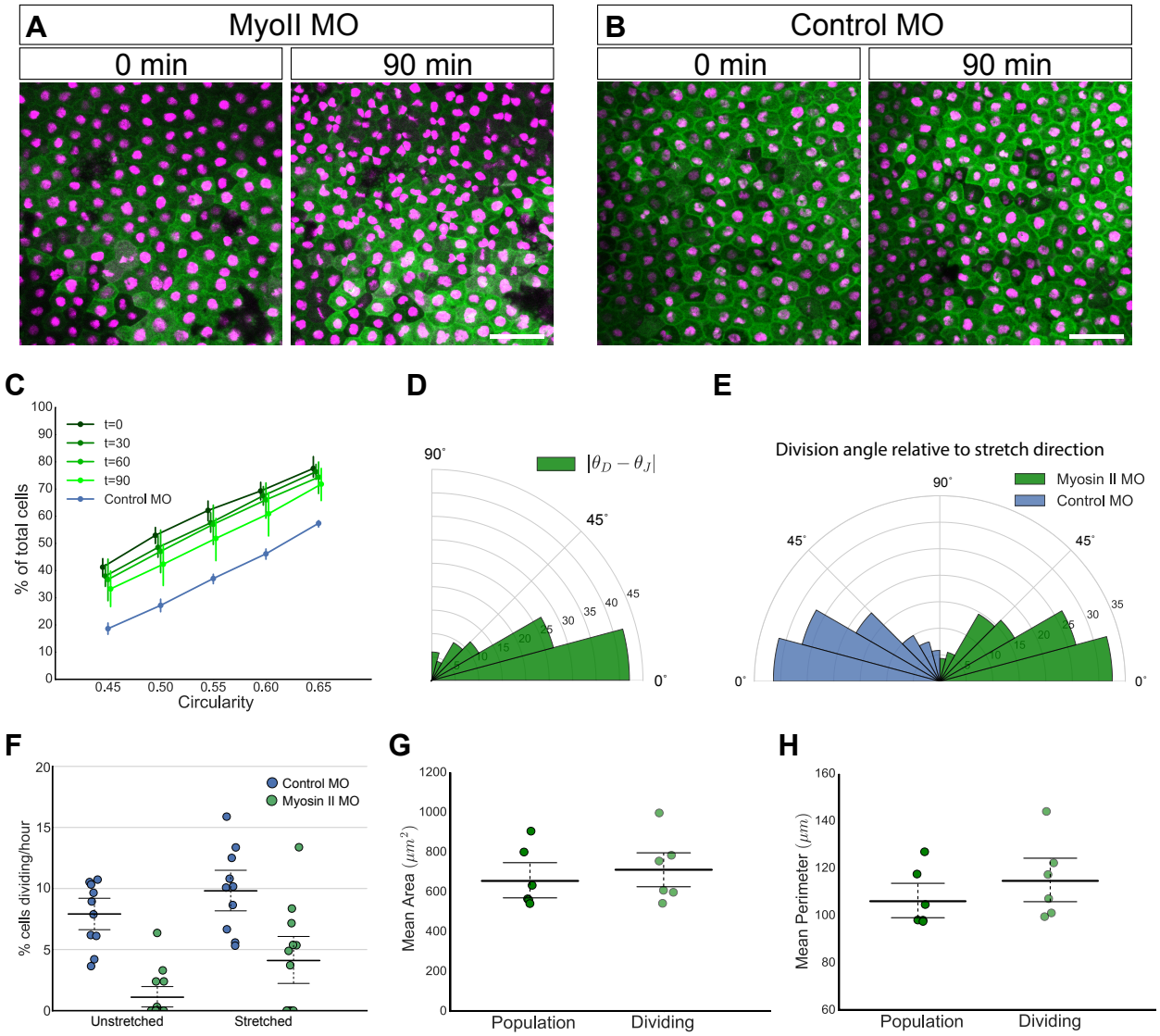


**Figure 6: Myosin II MO cells maintain alignment of division to tricellular junctional shape, but have perturbed proliferation rate. A.** Images taken from a confocal timelapse movie of stretched myosin II morpholino injected animal cap explants at 0 and 90 minute intervals. Butterfly nuclei seen prominently at 90 minutes, where nuclei are in contact. **B.** Timelapse images of control morpholino-injected stretched animal cap explants at 0 and 90 minute intervals. **C.** Cumulative distribution of cell circularity defined by area, $C_A$, in myosin II MO knockdown stretched animal caps (shaded green) at t=0, 30, 60 and 90 minutes after stretch. Cumulative distribution for unstretched t=0 control MO knockdown experiments shown in blue. Error bars represent 95% confidence intervals. Error bars for myosin II MO t=90 minutes distribution does not overlap with control MO, indicating a significant difference from unstretched shape. Markers are slightly off-set for clarity. **D.** Rose plot of difference between division angle, $\theta_D$, and orientation of shape based on junctions, $\theta_J$, for 216 cells from myosin II knockdown stretched experiments. Mann-Whitney U test found significant alignment compared to random ($p < 5.72 \times 10^{-15}$), but no significant difference from equivalent dataset in control stretched experiments. Percentages of cells shown. **E.** Rose plot of division angle relative to direction for stretch for control MO (532 cells; blue) and myosin II MO (301 cells; green) experiments. Mann-Whitney U and Kolmogorov Smirnov test found no significant difference between the two. **F.** Division rate (percentage of total cells entering mitosis per hour) in unstretched and stretched tissue from myosin II MO (green; n=10 for unstretched and n=12 for stretched) and control MO (blue; n=13 for unstretched and n=10 for stretched) experiments. Error bars represent mean and 95% confidence intervals. **G.** Comparison of mean area of population of all cells vs dividing cells from stretched myosin II knockdown experiments. Error bars represent mean and 95% confidence intervals, which overlap, indicating no significant difference. **H.** Comparison of mean perimeter of population of all cells vs dividing cells from stretched myosin II knockdown experiments. Error bars represent mean and 95% confidence intervals, which overlap, indicating no significant difference. Scale bar in **A** and **B**: 100µm.

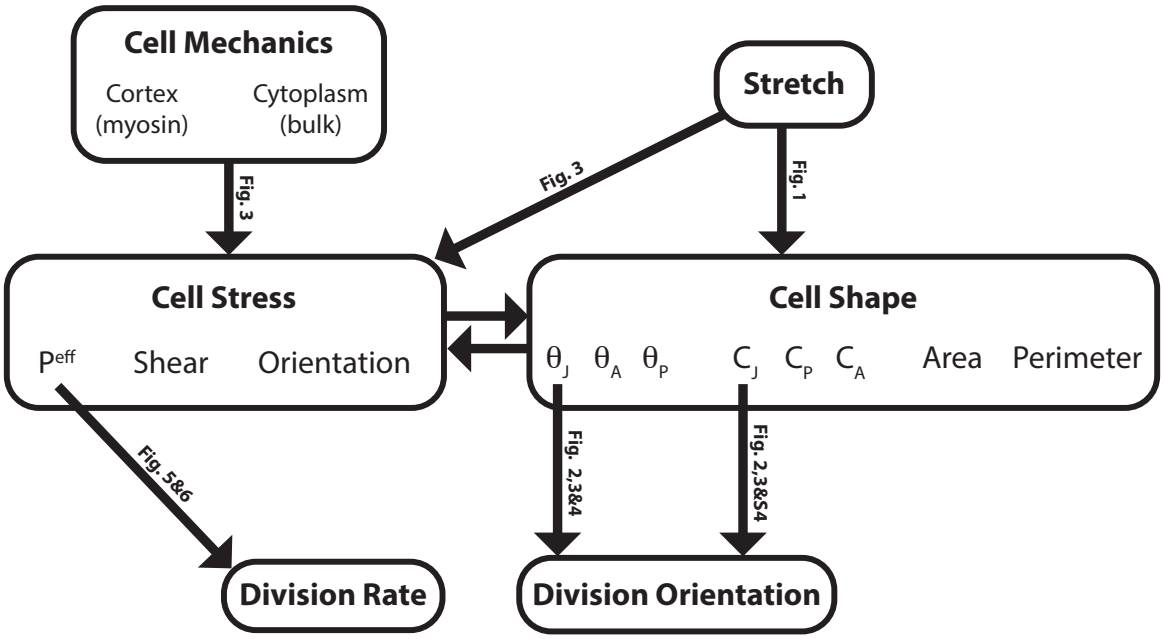


**Figure 7: Putative network summarizing proposed division mechanisms**. Rounded rectangles represent nodes of the network, with group names given in bold and sub-elements of the group written in regular font. Arrows represent lines of causality between nodes. Text along arrows reference Figures with data indicating that there is a causal link between two nodes or elements. Arrows connected to the boundary of a node indicate a causal link to/from all elements in the node. Arrows from sub-elements indicate the link is specifically only to/from the sub-element.